Propagation and Imaging of Mechanical Waves in a Highly Stressed Single-Mode Acoustic Waveguide

E. Romero, R. Kalra, N.P. Mauranyapin,* C.G. Baker, C. Meng, and W.P. Bowen
ARC Centre for Engineered Quantum Systems, School of Mathematics and Physics, The University of Queensland, Brisbane, Queensland 4072, Australia

(Received 12 February 2019; revised manuscript received 10 May 2019; published 14 June 2019)

We demonstrate a single-mode acoustic waveguide that enables robust propagation of mechanical waves. The waveguide is a highly stressed silicon-nitride membrane that supports the propagation of out-of-plane modes. In direct analogy to rectangular microwave waveguides, there exists a band of frequencies over which only the fundamental mode is allowed to propagate, while multiple modes are supported at higher frequencies. We directly image the mode profiles using optical heterodyne vibration measurement, showing good agreement with theory. In the single-mode frequency band, we show low-loss propagation (approximately 1 dB/cm) for an approximately 5-MHz mechanical wave. This design is well suited for acoustic circuits interconnecting elements such as nonlinear resonators or optomechanical devices for signal processing, sensing, or quantum technologies.

DOI: 10.1103/PhysRevApplied.11.064035

I. INTRODUCTION

Advances in nanoelectromechanical systems [1], optomechanics [2], and quantum computation [3] have fueled a resurgence in the field of acoustic circuits. The field is motivated by the prospect to generate, route, interact, and interface acoustic waves in on-chip architectures. While individual micromechanical devices have long been used for applications including signal processing [4], frequency control [5], and sensing [6], complex acoustic circuits remain a challenge. Such circuits could perform efficient acoustic information processing [7] with potentially low power consumption [8] and robustness in radiation harsh environments [9]. Recent work has also explored acoustic circuits in quantum technologies [10–12], hybrid optomechanical systems [13,14], and topological metamaterials [15].

Large-scale acoustic circuits require that the acoustic waves be reliably guided between the various components in the circuit. Waveguides for electromagnetic waves at optical, microwave, and radio frequencies are mature technologies, having overcome issues of loss, scattering, and dispersion. Acoustic waveguides, on the other hand, are still an active area of research [16–19]. The variety of channels through which mechanical vibrations can propagate represents a challenge for acoustic waveguides, where imperfections can scatter energy into other modes.

One key lesson from electromagnetic waveguides is that robust low-loss signal propagation is much easier to achieve when the waveguide is operated in a frequency band where only a single mode is available. This is evident in the use of the dominant TE_{10} mode in rectangular microwave waveguides and in single-mode optical fibers, which have enabled the long-distance communication that forms the backbone of the internet. Here, we translate this concept to acoustics, demonstrating a low-loss single-mode acoustic waveguide.

Recently, Patel *et al.* [20] reported the first single-mode phononic waveguide, characterizing it through its coupling with an optomechanical resonator. The waveguide comprised of a nanoscale silicon beam supported by a phononic crystal, which serves to confine energy to the beam and modify its mode structure to create a single-mode frequency band. However, acoustic waveguides based on phononic crystals offer a limited bandwidth for acoustic confinement determined by the lattice constant of the periodic array. Additionally, propagating phonons can couple to different polarizations such as longitudinal, shear, surface, or transversal. The coupling from one acoustic branch to the other causes scattering, which generates losses. In contrast, we demonstrate single-mode operation with a membrane, which inherently eliminates all but out-of-plane modes in the frequency range of interest. By restricting the acoustic modes available in the system, it is possible to engineer a single-mode frequency region.

To further enhance the acoustic propagation, we fabricate the single-mode waveguide with a highly stressed material. The tensile stress in the membrane increases the speed of sound without adversely affecting the loss rate, a long-known technique in micromechanical systems called *dissipation dilution* [21]. These two main characteristics

*n.mauranyapin@uq.edu.au

have allowed us to build a single-mode acoustic waveguide with low-loss propagation (approximately 1 dB/cm) while operating in vacuum and room temperature. Our waveguides exhibit a reduction of losses at least one order of magnitude compared with the state-of-the-art phononic waveguides in the MHz frequency range [16] and comparable with phononic waveguides operated in cryogenic environments [20]. This design is motivated by increasing interest in developing acoustic circuits based on interconnecting multiple micro or nanoscale resonators [16,22–24]. We characterize the waveguides using optical heterodyne vibration measurement to directly image the modes, demonstrating good agreement with theory.

II. THEORY

We consider a waveguide made of a highly stressed rectangular membrane with width L_x and length L_y. The membrane extends along the y direction, the direction of propagation, with $L_y \gg L_x$ as illustrated in Figs. 1(a)–1(c). The acoustic impedance mismatch between the membrane and the supporting bulk material serves to confine the energy within the membrane [25].

Vibrations of a membrane, where the restoring force is dominated by stress as opposed to the flexural rigidity of the material, satisfy the following wave equation [21]:

$$\sigma \nabla^2 u(x,y,t) - \rho \frac{\partial^2}{\partial t^2} u(x,y,t) = 0, \tag{1}$$

where $u(x,y,t)$ is the displacement field along the out-of-plane direction z, σ is the tensile stress of the membrane, and ρ is the density of the membrane material. The boundary conditions enforced by the clamping to the substrate are $u(0,y,t) = u(L_x,y,t) = 0$. The solution for the out-of-plane vibrations of the membrane driven at frequency Ω is [26]

$$u(x,y,t) = \sum_n u_n \phi_n(x) \phi(y) e^{-i(\Omega t + \theta_n)}, \tag{2}$$

where u_n and θ_n are the amplitude and phase of the nth transverse mode, respectively, $\phi_n(x) = \sin(k_x x)$ is the transverse mode shape with $k_x = n\pi/L_x$, and $\phi(y) = e^{\pm i k_y y}$ is the propagating wave. The value of k_y is obtained from the dispersion relation as derived from the wave equation,

$$\Omega(k_y) = \sqrt{\frac{\sigma}{\rho}} \sqrt{k_y^2 + \left(\frac{n\pi}{L_x}\right)^2}. \tag{3}$$

We see from the dispersion relation that each transverse mode n has a cutoff frequency $\Omega_{c,n} = \sqrt{\sigma/\rho}\,(n\pi/L_x)$ below which that mode cannot propagate. Thus, there is a frequency band over which the waveguide is single mode, where $\Omega_{c,1} < \Omega < \Omega_{c,2}$. This result is shown in Fig. 1(d), where we plot the dispersion relation calculated for a silicon-nitride membrane with width $L_x = 76$ μm, thickness $h = 80$ nm, density $\rho = 3184$ kg/m^3, and internal tensile stress $\sigma = 1$ GPa. Highlighted in gray is the frequency band where there are no modes available for propagation, while the single-mode region is highlighted in blue.

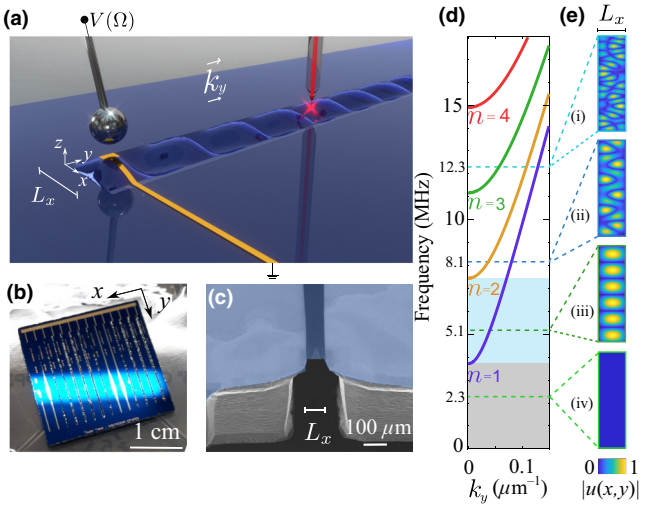

FIG. 1. (a) Illustration of the acoustic waveguide with width L_x and length L_y. The four boundaries of the rectangular waveguide are fixed by the substrate. The waveguide is actuated electrostatically through a capacitor formed by an on-chip fabricated electrode on top of the membrane (shown in gold) and a probe electrode (in silver). The oscillations represent mechanical waves propagating along y with wave vector $\vec{k}_y$. These waves are detected using a lensed optical fiber through the phase modulation of the laser light reflected back into the fiber. (b) Image of a chip with 14 waveguides in parallel, four of which are intact. (c) False color cross-sectional scanning electron micrograph of a cut of the released Si_3N_4 membrane (blue) held by the Si substrate (gray). (d) Calculated dispersion relation for the waveguide, showing the first four mode branches. Shaded in blue and gray are the frequency bands corresponding to the single-mode region and the band below cutoff, respectively. (e) Examples of two-dimensional amplitude mode profiles for a waveguide of finite length $|u(x,y)|$ calculated using Eq. (2). These resonance frequencies are indicated by dashed lines in (d) and correspond to the experimental results shown in Fig. 3.

In practice, we measure a waveguide with finite length that causes reflection from the boundary $y = 0$ and $y = L_y$. The two solutions for $\pm k_y$ result then in two counter-propagating waves. The two counter-propagating waves are equivalent to a standing wave with resonance frequency Ω_m in an infinite waveguide with longitudinal mode profile $\phi_m(y) = \sin(k_y y)$. In Fig. 1(e) we show examples of the two-dimensional profiles $|u(x,y)|$ fit to the experimental data shown in Fig. 3. In contrast to the

simple profile expected in the single-mode regime, the profiles at higher frequencies are a result of the interference between multiple modes and depend both on their relative amplitudes and phases with respect to the drive tone.

III. EXPERIMENTAL METHODS

A. Fabrication

The acoustic waveguides are fabricated from high-stress ($\sigma \sim 1$ GPa) low-pressure chemical-vapor-deposited Si_3N_4 films double-sided deposited on 500- μm Si wafers. They have dimensions $L_x = 75$–80 μm, $L_y \approx 1.8$ cm and thickness $h = 80$ nm. The fabrication process is illustrated in Fig. 2(a), with steps labeled [(i)–(vi)].

(i) The process begins with a silicon wafer double-side coated with a silicon-nitride thin film. (ii) Gold electrodes are patterned on the top side of the wafer using negative photoresist and a lift-off process. (iii) Both the top and bottom surfaces of the wafer are coated with 150 nm of aluminium followed by photoresist. The aluminium on the bottom side is patterned with photolithography and wet etched to serve as an etch mask. The photoresist and aluminium on the top side protects the surface during bottom-side patterning and etching, respectively. (iv) The exposed silicon nitride is etched using reactive ion etching (RIE) combining SF_6 and CF_4 gases. (v) The patterned aluminium is used as a mask for back-side etching of roughly 480 μm of silicon in the area below the membrane using deep reactive ion etching (DRIE). During the fabrication process, we avoid oxygen plasma cleaning due to the adverse effect known to affect the tensile stress in silicon-nitride films [27]. (vi) The removal of the remaining 20 μm of silicon and the aluminium film is done simultaneously with the final release of the silicon-nitride membrane using a highly concentrated potassium hydroxide (KOH) solution. The KOH etch of silicon is anisotropic and forms angled end facets following the Si(111) plane that finish the rectangular structure of our membrane. This process straightens the edges of the waveguide in a self-limiting process, as shown in Figs. 1(b) and 1(c).

B. Measurement setup

Measurements are performed at room temperature with the waveguide in a vacuum chamber with pressure $P \sim 10^{-7}$ mbar [28]. The waveguide is actuated electrostatically through a capacitor formed by the on-chip electrode and a probe electrode held approximately 5 μm above the waveguide, as shown in Fig. 1(a). The force applied is proportional to $F \propto (V_{dc} + V_{ac}\cos\Omega t)^2$, where V_{dc} is the applied dc bias and V_{ac} is the amplitude of the ac drive at frequency Ω [29].

To measure the vibrations on the waveguide, we use an optical interferometric heterodyne detection scheme, represented in Fig. 2(b). A Ti:sapphire laser beam with wavelength $\lambda = 780$ nm is passed through an AOM driven at 77 MHz to obtain a frequency-upshifted local oscillator beam as well as a nondiffracted probe beam at 780 nm. The probe beam is focused onto the membrane through a lensed fiber with spot size approximately 1 μm [Fig. 1(a)].

The membrane vibrations modulate the phase of the probe light reflected back into the lensed fiber, which interferes with the local oscillator to create beat notes at $\omega_{AOM} \pm \Omega$. With low-amplitude vibrations, the amplitude of the photocurrent at frequency $\omega_{AOM} \pm \Omega$ is, to a good approximation, directly proportional to the amplitude of vibration of the membrane $|u(x,y)|$. We use a spectrum analyzer for measurement of the photocurrent at frequency $\omega_{AOM} + \Omega$ to obtain the mechanical response. Both the electrode and lensed fiber are mounted

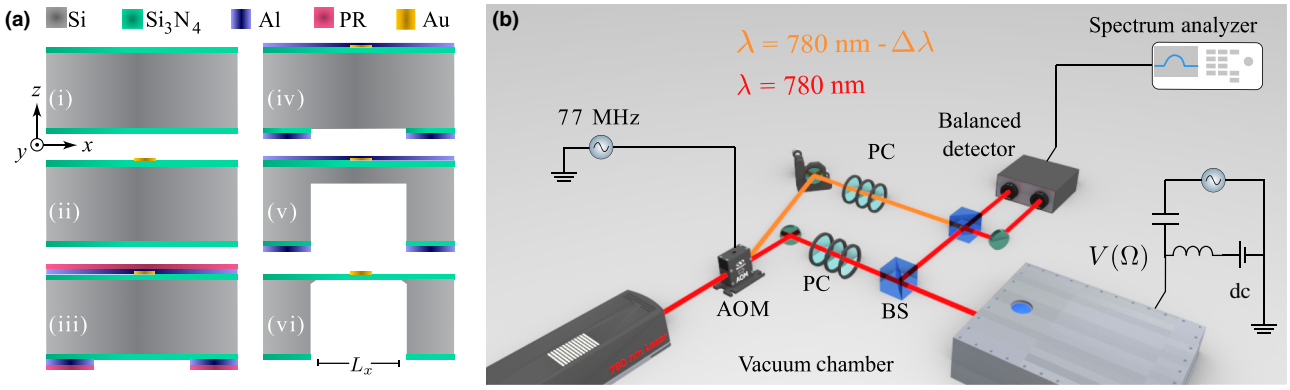

FIG. 2. (a) Fabrication process for the acoustic waveguides described in Sec. III A. The process requires silicon (Si), silicon nitride (Si_3N_4), aluminium (Al), photoresist (PR) and gold (Au). The perspective of the scheme represents the lateral cut along x of a membrane waveguide with width L_x. (b) Schematic of the optical heterodyne detection setup. The optical setup is composed by an acousto-optical modulator (AOM), polarization controllers (PC), and beam splitters (BS), used to measure the mechanical vibrations of the waveguide. The diffracted local oscillator (orange) and nondiffracted probe beams (red) are combined in a final beam splitter for balanced photodetection. The actuation voltage $V(\Omega)$ is applied to the waveguide in the vacuum chamber via a feedthrough.

on piezoelectric positioners to allow them to be scanned during measurement.

IV. RESULTS

A. Mode shape imaging

In a first experiment, we image the transverse-mode shape while the membrane is continuously actuated at a frequency Ω. This is repeated at different frequencies lying within the bands below cutoff, in the single-mode region and in the multimode region, as marked by the dashed lines in the plot of the dispersion relationship, Fig. 1(b). Two scenarios are possible.

Given the finite length of the waveguide ($L_y \approx 1.8$ cm), standing waves are generated if the propagation and reflection losses are sufficiently low. If the losses are high, however, propagating waves are observed, which are not significantly perturbed by reflections at the end of the waveguide. While the two cases result in similar profiles, we know from experiments presented in the next section that standing waves are generated. We thus restrict our discussion of mode profiles to those corresponding to standing waves.

To image the transverse-mode shape, the photocurrent at frequency $\omega_{\mathrm{AOM}} + \Omega$ is recorded while the lensed fiber is scanned over the width of the waveguide. The scan has an average speed of 1 μm/s with a 200-nm step size. The measured profiles for actuation at $\Omega/2\pi = 12.3$, 8.1, 5.1, and 2.3 MHz, are shown in Figs. 3(i), 3(ii), 3(iii), and 3(iv) respectively. As expected, the waveguide does not respond when driven at 2.3 MHz, well below the expected cutoff frequency of 3.7 MHz, as shown in Figs. 1(d) and 1(e). Driving in the single-mode frequency band results in the expected fundamental transverse-mode shape $|u(x,y)| \propto \sin(\pi x/L_x)$ with amplitude fitted from Eq. (2), shown in red in Fig. 3(iii). The measured photocurrent amplitude of approximately 1 μA corresponds to an actual vibration amplitude of approximately 10 pm.

With a frequency drive of 8.1 and 12.3 MHz, the waveguide supports two and three modes, respectively. The two and three antinode character of the $n = 2$ and $n = 3$ modes is clearly visible in Figs. 3(ii) and 3(i). The theoretical fitting represented as red lines in Fig. 3 is obtained using Eq. (2) with the relative amplitudes and phases as the free parameters of each standing wave in a finite-length waveguide. For example, the experimental results shown in Fig. 3(ii) correspond to a frequency drive of $\Omega/2\pi = 8.1$ MHz. In this case, the acoustic modes $n = 1$ and $n = 2$ are expected to have longitudinal wavelengths $\lambda_{y,1} = 2\pi/k_{y,1} = 76$ μm and $\lambda_{y,2} = 2\pi/k_{y,2} = 169$ μm, respectively. The relative modal amplitudes and phases are obtained by fitting the experimental data Fig. 3(ii), obtaining $\theta_2 - \theta_1 = 1.3$ rad and $u_2/u_1 = 1.8$. These results agree very well with the calculated mode shapes we expect from perfect standing waves.

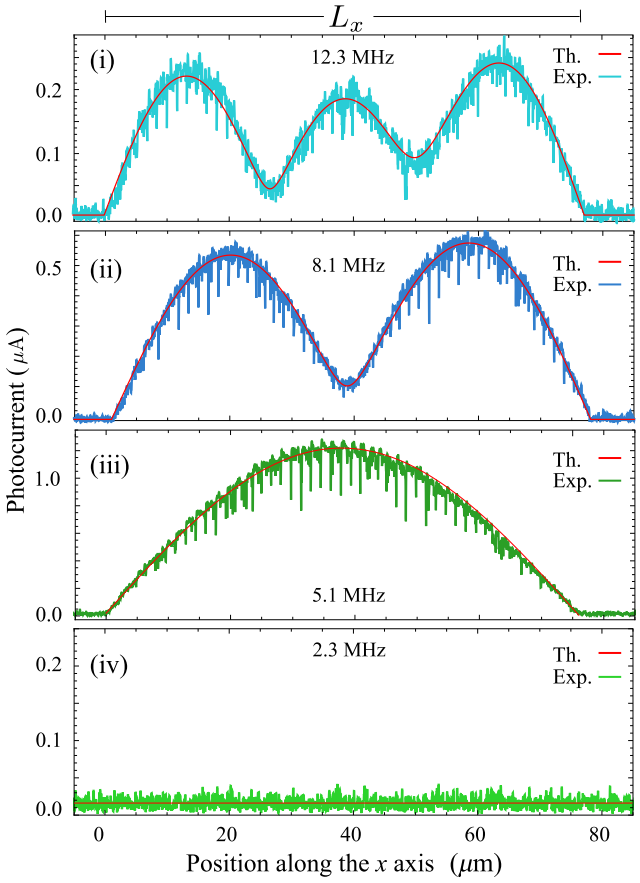

FIG. 3. (i)–(iv) Experimentally measured transverse-mode profiles of the acoustic waveguide when actuated at (i) $\Omega/2\pi = 12.3$ MHz, (ii) $\Omega/2\pi = 8.1$ MHz, (iii) $\Omega/2\pi = 5.1$ MHz, and (iv) $\Omega/2\pi = 2.3$ MHz. The photocurrent at frequency $\omega_{\mathrm{AOM}} + \Omega$ is plotted as a function of the fiber's lateral position x while it is scanned across the waveguide of width $L_x \approx 76$ μm. The fiber is positioned approximately 3 mm from the actuation electrodes along the y axis, which corresponds to the direction of propagation. The red curves are the theoretical fit for the transverse-mode profile $|u(x,y)|$ calculated with Eq. (2), which are displayed in Figs. 1(d) and 1(e). The color of each plot corresponds to the color of the dashed lines in Fig. 1(e), indicating the (iv) zero-, (iii) one-, (ii) two-, and (i) three-mode frequency bands.

Over a timescale of minutes, we observe relative phase drifts. To show this, we drive the waveguide at frequency $\Omega/2\pi = 10.2$ MHz, exciting the $n = 1$ and $n = 2$ modes. We measure the transverse-mode shape as done before, repeating this at the same y position over the time span of a few minutes. In Fig. 4(a), we show three modes where we fit the phase difference between modes. The phase difference of the first measurement (i) $\theta_2 - \theta_1 = 4.27$ rad (blue), the second (ii) $\theta_2 - \theta_1 = 4.02$ rad (red), and third (iii) $\theta_2 - \theta_1 = 2.76$ rad (purple). The first two measurements are taken consecutively while the third measurement is taken minutes after.

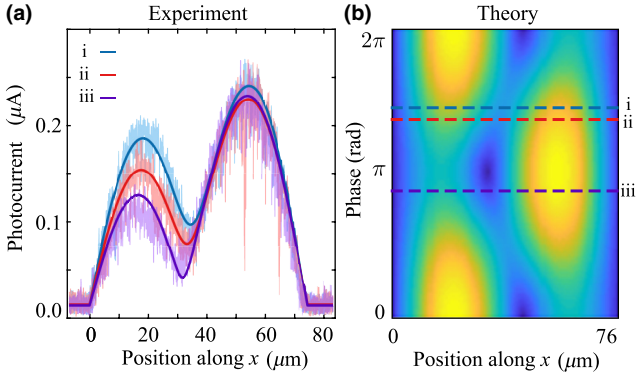

FIG. 4. (a) Consecutive measurements of the transverse-mode profile of the waveguide actuated at a fixed frequency $\Omega/2\pi = 10.12$ MHz and position along the y axis. The three mode profiles, (i) blue, (ii) red, and (iii) purple are measured in that chronological order. These measurements demonstrate that the mode shape changes over time. The solid lines are the theoretical fit to the transverse-mode profile $|u(x,y)|$. (b) Theoretical lateral and transverse-mode profile $|u(x,y)|$ as a function of the relative phase between the $n = 1$ and $n = 2$ modes for a given position along y. The relative amplitudes are $u_2/u_1 = 3.3$. The theoretical fit for each measurement in (a) correspond to a phase-difference value displayed here. The phase difference for each measurement is (i) $\theta_2 - \theta_1 = 4.27$ rad, (ii) $\theta_2 - \theta_1 = 4.02$ rad, and (iii) $\theta_2 - \theta_1 = 2.76$ rad.

We associate the change in the mode shape to be caused by a relative phase drift between the $n = 1$ and $n = 2$ modes. In Fig. 4(b), we plot the theoretical interference pattern produced by the first two modes as a function of the relative phase between them. We fit the relative phase between the first two modes to the experimental data shown in Fig. 4(a), where the fit is color coded with dashed lines. While we do not know the exact mechanism causing the phase drifts, we suspect that thermal effects are at play. The measurement protocol involves optical power approximately equal to the 100-μW laser directed at the membrane, which is housed in a vacuum chamber at $P \sim 10^{-7}$ mbar. Poor thermalization may lead to temperature rising, potentially modifying the local elastic properties of the membrane. Given that the membranes exhibit resonances with high-quality factor, slight changes in the resonance condition produce a large change in the relative phase. These effects become more evident when multiple modes are driven simultaneously.

B. Frequency response

To characterize the frequency response of the acoustic waveguide, we perform a network analysis with the fiber positioned at the center of the waveguide while sweeping the drive frequency Ω from $\Omega/2\pi = 1$ to $\Omega/2\pi = 10$ MHz. As seen from the blue data in Fig. 5(a), the mechanical signal is greatly suppressed at low frequencies. The 3-dB cutoff at $\Omega_{c,1}/2\pi = 3.8$ MHz is consistent

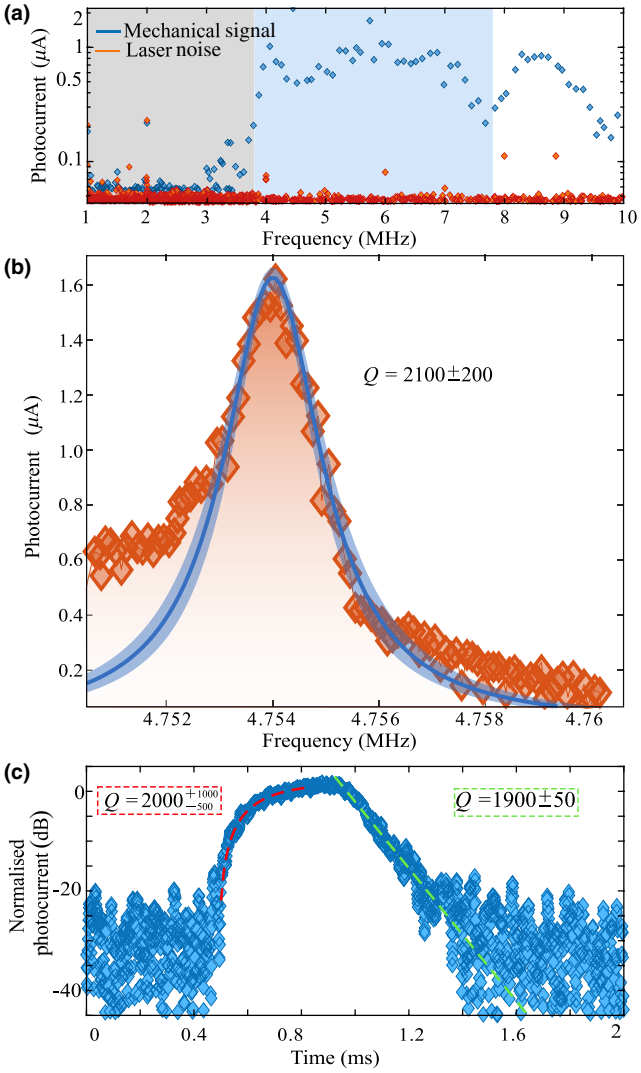

FIG. 5. (a) Network analysis of the mechanical waveguides. The mechanical signal (blue) decreases to the laser noise level (orange) in the forbidden band (shaded gray background), which corresponds to the frequency band below the cutoff frequency $\Omega < \Omega_{c,1}$. The single-mode frequency band is represented as the blue shaded region $\Omega_{c,1} < \Omega < \Omega_{c,2}$. (b) Frequency response of the waveguide highlighting a resonance at $\Omega_m/2\pi = 4.754$ MHz (orange dots). The peak is fit to a Lorentzian (in blue with the shading denoting uncertainty) from which we extract a quality factor $Q = 2100 \pm 200$. (c) Response of the waveguide to a 5-ms pulse at 4.754 MHz (blue dots). The normalized photocurrent is plotted in decibels from which the ring-up and ring-down times are extracted using curve fitting. The resulting fitting curves are shown in red and green for the ring up and ring down, yielding quality factors of $Q = 2000^{+1000}_{-500}$ and 1950 ± 50, respectively.

with the theoretical cutoff frequency $\Omega_{c,1}/2\pi = 3.7$ MHz calculated from Eq. (3). The laser noise level is shown in orange in Fig. 5(a) for reference. The response above cutoff is populated with resonant peaks that drift on the timescale

of minutes, consistent with observations presented in Fig. 4. To capture the linewidth Γ_m of an individual resonance at frequency Ω_m, we repeat the measurement over a narrow frequency window and shorter time than the drift. Figure 5(b) shows a measurement at one resonance frequency $\Omega_m/2\pi = 4.754$ MHz, which is in the single-mode frequency band. Fitting this peak to a Lorentzian, whose symmetry is broken by the presence of another resonance at lower frequency, we estimate a quality factor of $Q = \Omega_m/\Gamma_m = 2100 \pm 200$.

C. Pulsed actuation

In order to provide another measure of the quality factor of the resonance at $\Omega_m/2\pi = 4.754$ MHz, we perform ring-up and ring-down measurements. With the fiber positioned 8.8 mm away from the actuation electrodes, we gate the drive tone with a square pulse with a width chosen to be longer than the expected ring-up time of the cavity. In order to resolve this dynamics we acquire data with a resolution bandwidth ranging from 100 kHz to 1 MHz, corresponding to a integration time of 1–10 μs. To improve the signal-to-noise ratio, we average over 2000 repetitions synchronized to an external trigger. Figure 5(c) shows the normalized photocurrent as a function of time.

The ring up at the start of the pulse is fitted to the expected exponential build up for a driven harmonic oscillator, from which we extract a quality factor of $Q = 2000^{+1000}_{-500}$. The ring down at the end of the pulse is fitted to an exponential decay, which yields $Q = 1950 \pm 50$, in fair agreement with our other estimates of Q.

The measured quality factor Q is easily related to the propagation loss $\alpha = \Gamma_m/v$, where the speed of sound in the membrane is given by $v = \partial\Omega(k_y)/\partial k_y \propto \sqrt{\sigma/\rho}$. With $Q \approx 1900$, we estimate $\alpha < 1$ dB/cm. This estimate is a conservative value since it neglects the fact that imperfect reflections at the ends of the cavity can also contribute to the measured decay rate of the cavity. Nevertheless, it compares favorably to previous reports of room-temperature megahertz waveguides [16]. The improvement propagation dissipation exhibited by our waveguides relies upon the fact that the membranes are under high tensile stress.

As previously shown for membrane resonators [21,30], high tensile stress increases the quality factor $Q = \Omega_m/\Gamma_m$ by increasing the resonance frequency Ω_m of the resonator without adversely affecting the loss rate Γ_m. This effect, known as dissipation dilution is directly applied to the propagation loss in a waveguide α by increasing the speed of sound on the membrane.

V. CONCLUSION

In this work we demonstrate a single-mode acoustic waveguide based on a highly stressed silicon-nitride membrane. Direct imaging of the mode shapes in the single- and multimode regions show good agreement with the analytical solutions of the system. The finite-length waveguide we measure has sufficiently low propagation loss and reflection from the end surfaces to behave as a resonator with a quality factor approximately 2000 in the single-mode region. The combination of the single-mode region and the highly stressed material allows us to develop a single-mode acoustic waveguide with low propagation loss in which the conservative estimate of $\alpha \sim 1$ dB/cm represents an order of magnitude lower than previous room-temperature acoustic waveguides operating at megahertz frequencies [16]. The waveguide is the first step towards developing scalable acoustic circuits, which may find application in sensing [31], computation [8], and even quantum technologies [10–14].

The structural and mathematical similarity of our implementation to microwave and optical waveguides paves a direct path towards developing other circuit components. The inclusion of additional degrees of freedom such as electronic actuation through interdigitated transducers could also, for instance, be employed to modulate the speed of sound through changes in the effective tension. It is possible to encourage, in future, complex acoustic circuits built from acoustic waveguides, processing and communicating information, interconnecting nanomechanical sensors, interfacing to photonic and microwave systems and, generally, providing new capabilities for on-chip classical and quantum-information systems.

ACKNOWLEDGMENTS

This research is primarily funded by the Australian Research Council and Lockheed Martin Corporation through the Australian Research Council Linkage Grant No. LP160101616. Support is also provided by the Australian Research Council Centre of Research Excellence for Engineered Quantum Systems (CE170100009). R.K., C.G.B., and W.P.B. acknowledge fellowships from the University of Queensland (UQFEL1719237 and UQFEL1833877) and the Australian Research Council (FT140100650), respectively. This work is performed in part at the Queensland node of the Australian National Fabrication Facility, a company established under the National Collaborative Research Infrastructure Strategy to provide nano and microfabrication facilities for Australia's researchers. The authors thank Luke Uribarri, George Brawley, and Hafiz Abdullah for useful discussions, and Doug Mair and Kai-Yu Liu for technical assistance.

E.R. and R.K. contributed equally to this work.

[1] K. L. Ekinci and M. L. Roukes, Nanoelectromechanical systems, Rev. Sci. Instrum. **76**, 061101 (2005).

[2] Markus Aspelmeyer, Tobias J. Kippenberg, and Florian Marquardt, Cavity optomechanics, Rev. Mod. Phys. **86**, 1391 (2014).

[3] Thaddeus D. Ladd, Fedor Jelezko, Raymond Laflamme, Yasunobu Nakamura, Christopher Monroe, and Jeremy Lloyd O'Brien, Quantum computers, Nature **464**, 45 (2010).

[4] Robert Aigner, in *Ultrasonics Symposium, 2008. IUS 2008. IEEE* (IEEE, Beijing, China, 2008) p. 582.

[5] J. T. M. Van Beek and R. Puers, A review of MEMS oscillators for frequency reference and timing applications, J. Micromech. Microeng. **22**, 013001 (2011).

[6] Robert Bogue, Recent developments in MEMS sensors: A review of applications, markets and technologies, Sens. Rev. **33**, 300 (2013).

[7] Sophia R. Sklan, Splash, pop, sizzle: Information processing with phononic computing, AIP Adv. **5**, 053302 (2015).

[8] M. L. Roukes, in *Electron Devices Meeting, 2004. IEDM Technical Digest. IEEE International* (IEEE, San Francisco, CA, USA, 2004) p. 539.

[9] Faisal K. Chowdhury, Daniel Saab, and Massood Tabib-Azar, Single-device "XOR" and "AND" gates for high speed, very low power LSI mechanical processors, Sens. Actuators A Phys. **188**, 481 (2012).

[10] Rusko Ruskov and Charles Tahan, On-chip cavity quantum phonodynamics with an acceptor qubit in silicon, Phys. Rev. B **88**, 064308 (2013).

[11] S. J. M. Habraken, K. Stannigel, M. D. Lukin, P. Zoller, and P. Rabl, Continuous mode cooling and phonon routers for phononic quantum networks, New J. Phys. **14**, 115004 (2012).

[12] Benoît Vermersch, P.-O. Guimond, Hannes Pichler, and Peter Zoller, Quantum State Transfer via Noisy Photonic and Phononic Waveguides, Phys. Rev. Lett. **118**, 133601 (2017).

[13] Heedeuk Shin, Jonathan A. Cox, Robert Jarecki, Andrew Starbuck, Zheng Wang, and Peter T. Rakich, Control of coherent information via on-chip photonic–phononic emitter–receivers, Nat. Commun. **6**, 6427 (2015).

[14] Krishna C. Balram, Marcelo I. Davanço, Jin Dong Song, and Kartik Srinivasan, Coherent coupling between radiofrequency, optical and acoustic waves in piezo-optomechanical circuits, Nat. Photonics **10**, 346 (2016).

[15] Jinwoong Cha, Kun Woo Kim, and Chiara Daraio, Experimental realization of on-chip topological nanoelectromechanical metamaterials, Nature **564**, 229 (2018).

[16] D. Hatanaka, I. Mahboob, K. Onomitsu, and H. Yamaguchi, Phonon waveguides for electromechanical circuits, Nat. Nanotechnol. **9**, 520 (2014).

[17] Kejie Fang, Matthew H. Matheny, Xingsheng Luan, and Oskar Painter, Optical transduction and routing of microwave phonons in cavity-optomechanical circuits, Nat. Photonics **10**, 489 (2016).

[18] M. Ghasemi Baboly, C. M. Reinke, B. A. Griffin, I. El-Kady, and Z. C. Leseman, Acoustic waveguiding in a silicon carbide phononic crystals at microwave frequencies, Appl. Phys. Lett. **112**, 103504 (2018).

[19] Yangyang Liu, Nathan Dostart, and Milš A. Popović, in *2016 Conference on Lasers and Electro-Optics (CLEO)* (IEEE, San Jose, CA, USA, 2016) p. 1.

[20] Rishi N. Patel, Zhaoyou Wang, Wentao Jiang, Christopher J. Sarabalis, Jeff T. Hill, and Amir H. Safavi-Naeini, Single-Mode Phononic Wire, Phys. Rev. Lett. **121**, 040501 (2018).

[21] Silvan Schmid, Luis Guillermo Villanueva, and Michael Lee Roukes, *Fundamentals of Nanomechanical Resonators* (Springer International Publishing, Switzerland, 2016).

[22] I. Mahboob, E. Flurin, K. Nishiguchi, A. Fujiwara, and H. Yamaguchi, Interconnect-free parallel logic circuits in a single mechanical resonator, Nat. Commun. **2**, 198 (2011).

[23] Josef-Stefan Wenzler, Tyler Dunn, Tommaso Toffoli, and Pritiraj Mohanty, A nanomechanical Fredkin gate, Nano Lett. **14**, 89 (2014).

[24] Warren Fon, Matthew H. Matheny, Jarvis Li, Lev Krayzman, Michael C. Cross, Raissa M. D'Souza, James P. Crutchfield, and Michael L. Roukes, Complex dynamical networks constructed with fully controllable nonlinear nanomechanical oscillators, Nano Lett. **17**, 5977 (2017).

[25] B. Graczykowski, J. Gomis-Bresco, F. Alzina, J. S. Reparaz, A. Shchepetov, M. Prunnila, J. Ahopelto, and C. M. Sotomayor Torres, Acoustic phonon propagation in ultra-thin Si membranes under biaxial stress field, New J. Phys. **16**, 073024 (2014).

[26] Martin Redwood, *Mechanical Waveguides* (Pergamon Press, Oxford, 1960).

[27] Niklas Luhmann, Artur Jachimowicz, Johannes Schalko, Pedram Sadeghi, Markus Sauer, Annette Foelske-Schmitz, and Silvan Schmid, Effect of oxygen plasma on nanomechanical silicon nitride resonators, Appl. Phys. Lett. **111**, 063103 (2017).

[28] Andreas Naesby, Sepideh Naserbakht, and Aurélien Dantan, Effects of pressure on suspended micromechanical membrane arrays, Appl. Phys. Lett. **111**, 201103 (2017).

[29] Christiaan Bekker, Rachpon Kalra, Christopher Baker, and Warwick P. Bowen, Injection locking of an electro-optomechanical device, Optica **4**, 1196 (2017).

[30] S. Schmid, K. D. Jensen, K. H. Nielsen, and A. Boisen, Damping mechanisms in high-Q micro and nanomechanical string resonators, Phys. Rev. B **84**, 165307 (2011).

[31] Jean C. Coulombe, Mark C. A. York, and Julien Sylvestre, Computing with networks of nonlinear mechanical oscillators, PLoS One **12**, e0178663 (2017).